



Smelting Vanadium–Titanium Magnetite by OY Furnace: Effect of Prereduction Degree on the Softening, Melting, and Dropping Behavior of Direct Reduction Iron in Melter Gasifier

CHEN YIN, SHENGFU ZHANG, KUNYU MA, WANPENG DONG, MEILONG HU, LIANGYING WEN, and CHENGUANG BAI

OY furnace, an improvement of COREX, is the vigorously developed environmentally friendly iron-making process. However, it has a higher fuel ratio than blast furnace. The high prereduction degree (PRD) of direct reduction iron (DRI) is beneficial to decrease the fuel consumption of OY furnace but also affect the softening, melting, and dropping properties of DRI in the final reduction process. In the study, the qualitative and quantitative relationships between the PRD (60 to 90 pct) and the softening, melting, and dropping behavior of the V–Ti-bearing DRI under the simulated OY furnace conditions were investigated. Results indicated that the increase in PRD of DRI improved its creep resistance, increasing its end temperature of softening (T_{40}). However, it also accelerated the reduction of TiO_2 to TiC and the slag foaming, which led to an increase in the melting temperature (T_S) and the dropping temperature (T_D). The slag foaming temperature (T_F) was declined from 1504 °C to 1441 °C as the PRD of DRI increasing from 60 to 90 pct, which inhibited the liquid permeability of the V–Ti-bearing bed, resulting in the deterioration of the dropping rates of molten iron and slag from 96.7 and 86.9 to 25.2 and 12.8 pct, respectively. In addition, the gas permeability of the V–Ti-bearing bed was also decreased due to the generated TiC and slag foaming. The maximum pressure drop (P_{Peak}) and gas permeability index (S_D) of the pressure drop curve after temperature T_F were multiplied from 8.06 kPa and 218.41 kPa °C to 20.14 kPa and 1324.17 kPa °C, respectively. Therefore, the V–Ti-bearing DRI with higher PRD is more likely to foam in the semi-coke bed, which is not recommended for the smelting of OY furnace.

<https://doi.org/10.1007/s11663-023-02739-y>

© The Minerals, Metals & Materials Society and ASM International 2023

I. INTRODUCTION

CURRENTLY, more than 70 pct of the global pig iron production (about 1.28 billion tons in 2021) is made through blast furnace process by using carbon as a reductant, whereas each ton of pig iron produced by this process discharges about 2.1 tons of CO_2 .^[1–3] With the implementation of the global zero carbon emission

strategy, the low carbon iron-making technology becomes an urgent need and has made considerable progress. OY furnace is a vigorously developed environmentally friendly iron-making process that uses O_2 instead of hot air to eliminate a lot of N_2 in the top gas.^[4,5] In the smelting process of OY furnace, CO , CO_2 , and H_2 are the main components of the top gas of the melter gasifier. Compared to blast furnace gas, the top gas with N_2 free in OY furnace helps separate and capture CO_2 . Therefore, despite its current high carbon consumption, it is still very attractive for the characteristics of good compatibility with CCUS (Carbon Capture, Utilization and Storage) and low coke demand.^[6–8]

The OY furnace is an improvement of COREX, mainly composed of the upper prereduction shaft furnace and the lower melter gasifier.^[4,5,9] The function of the melter gasifier is equivalent to the lower part of blast furnace to carry out the softening, melting, and further reducing of the DRI produced from the prereduction shaft furnace. PRD is an important index of DRI formed through gas–solid reduction of iron ore. In

CHEN YIN, KUNYU MA, and WANPENG DONG is with the College of Materials Science & Engineering, Chongqing University, Chongqing 400044, P.R. China. SHENGFU ZHANG, MEILONG HU, LIANGYING WEN, and CHENGUANG BAI are with the College of Materials Science & Engineering, Chongqing University and also with the Chongqing Key Laboratory of Vanadium-Titanium Metallurgy & Advanced Materials, Chongqing University, Chongqing 400044, P.R. China. Contact e-mail: zhangsf@cqu.edu.cn

Manuscript submitted October 30, 2022; accepted January 23, 2023.

Article published online February 27, 2023.

detail, assuming that all Fe in the iron ore at initial time is in the form of Fe_2O_3 , the ratio between the amount of oxygen removed to reach the oxygen content of the DRI and the oxygen of the iron ore at initial time is called PRD.^[32] Since the PRD of DRI has a crucial influence on the carbon consumption of OY furnace, it has become a concern for researchers and commercial factories.^[10–13] On the one hand, the lower PRD of DRI indicates that the gas exhausted from the melter gasifier into the shaft furnace is not fully utilized and a large amount of high-quality gas is wasted.^[14,15] On the other hand, the DRI with low PRD needs more gas and carbon for reduction when it enters melter gasifier, which not only decreases its dome temperature,^[9–11] weakening to the gas generated from the rapid pyrolysis of coal, but also increases the carbon consumption for direct reduction reaction of FeO ($\text{FeO} + \text{C} = \text{Fe} + \text{CO}$), causing deterioration of the gas permeability of semi-coke bed.^[16–18] Some calculations showed that the fuel ratio of OY furnace will increase by about 240 kg/thm when the PRD of DRI is decreased by 10 pct.^[19,20]

In addition, the PRD of DRI determines the fraction of FeO available as slag former and controls the thickness of metallic iron shell generated by reduction.^[21–23] As we all known, the thickness of the iron shell is proportional to the mechanical resistance it provides and the duration it holds for containing the liquid slag.^[21] With increased PRD, the content of FeO acting as a slag former is decreased, which in turn increases the liquid temperature of slag and reduces its quantity. This implies that higher PRD would lead to a higher softening and melting temperature.^[22,23] It is also found that as the PRD increases, the specified temperatures of the cohesive zone are gradually enhanced, and the temperature range is dwindled, meaning that the location of cohesive zone declines and the thickness becomes thinner than that at low PRD. As a result, the permeability of cohesive zone is promoted, which is beneficial to the stable production and operation for OY furnace.^[24]

So far, however, the V–Ti-bearing DRI with different PRDs as the charged burden of OY furnace has hardly been studied. It may adversely affect the running of melter gasifier to operate with high PRD when the V–Ti-bearing DRI is charged. The key to smelting vanadium–titanium magnetite is to prevent the over-reduction of TiO_2 and reduces the formation of TiC or Ti(C,N), which are the main driving force that causes slag thickening and foaming, and further deteriorates the bed permeability.^[25–29] FeO in the slag can effectively increase the oxygen potential of the slag and inhibit the reduction of TiO_2 ($2(\text{FeO}) + \text{TiC} = (\text{TiO}_2) + 2\text{Fe} + \text{C}$, $\Delta G^\theta = -313800 + 87.195T(\text{J/mol})$), but the increase of the PRD of DRI reduces the FeO content in the generated initial slag, resulting in an increase in TiC generation. When the volume fraction of TiC or Ti(C,N) in slag is increased from 0 to 6 vol pct, the viscosity of slag goes up about twice,^[30,31] which is detrimental to the smelting of vanadium–titanium magnetite.

In order to understand the effect of PRD on the reduction behavior of V–Ti-bearing DRI in the melter gasifier of OY furnace, the softening, melting, and dropping (SMD) behaviors of V–Ti-bearing DRI at varied PRDs were studied under simulated OY furnace conditions. The iron ore was prerduced in laboratory conditions. The mechanism of PRD on the SMD behavior was explained using wet chemical analysis, thermodynamic calculation (Factsage 8.0), and scanning electron microscopy (SEM). The vanadium yields in residual iron and dropping iron were also analyzed by inductively coupled plasma-optical emission spectroscopy (ICP-OES).

II. EXPERIMENTAL

A. Raw Materials

There were three kinds of iron ore (sinter, V–Ti-bearing pellet, and lump ore) and one kind of coke used in this study. All of the samples were sourced from the feedstock bin of an OY furnace. The particle sizes of iron ores and coke were ranged from 10 to 12.5 mm. The chemical compositions of iron ores are listed in Table I, and the proximate analysis and ultimate analysis of the coke are listed in Table II.

B. Prereduction Treatment of Mixed Iron Ore

The device used in the prereduction experiment was mainly composed of a high-temperature furnace with programmable temperature control and an electronic balance that records the weight online. The maximum temperature of the high-temperature furnace reaches 1400 °C. The accuracy of the electronic balance is 0.01 g, and the online recording interval is 0.5 s.

Firstly, the above three ores were dried and weighed according to the factory formula, including 240 g sinter, 236.25 g V–Ti-bearing pellet (VTP), and 23.75 g lump ore. Then they were evenly mixed and put into the reduction tank. During the experiment, 5 L/min of Ar was introduced to prevent the sample from oxidizing, and the heating rate was 10 °C/min before 850 °C. Subsequently, 15 L/min of reducing gas (30 pct CO + 70 pct Ar) was used for isothermal reduction at 850 °C. The reduction was terminated until the weight loss of the mixed iron ore reached the theoretical weight loss. Finally, the reducing gas was switched to 5 L/min of Ar to cool the reduced iron ores to room temperature. The theoretical weight loss of the sample with different PRDs was calculated by Eq. [1],^[32]

$$\Delta w = \left(\frac{R_t}{100} - \frac{0.111w_1}{0.43w_2} \right) * m_0 * 0.43w_2 / 100 \quad [1]$$

where Δw is the theoretical weight loss, g; R_t is the prereduction degree, pct; m_0 is the sample mass before reduction reaction, g; w_1 is the average FeO content in sample before reduction reaction, wt pct; w_2 represents the average total Fe content in sample before reduction reaction, wt pct.

Table I. Chemical Composition of Commercially Supplied Iron Ores

Samples	Proportion (wt pct)	TFe (wt pct)	FeO (wt pct)	SiO ₂ (wt pct)	CaO (wt pct)	MgO (wt pct)	Al ₂ O ₃ (wt pct)	TiO ₂ (wt pct)	V ₂ O ₅ (wt pct)	R ₂
Sinter	48.00	51.85	8.87	5.67	12.88	2.31	1.47	0.36	0.09	2.27
VTP	47.25	54.40	2.30	5.69	1.35	1.62	3.66	8.78	0.54	0.23
Lump ore	4.75	42.10	22.19	26.20	5.36	4.50	2.80	0.09	0.05	0.02
Average	—	52.59	6.40	6.65	7.07	2.09	2.57	4.33	0.30	1.06

VTP, V-Ti-bearing pellet. $R_2 = \text{wt pct (CaO)}/\text{wt pct (SiO}_2\text{)}$.

Table II. Basic Thermochemical Properties of Coke Sample

Samples	Proximate Analysis (Wt Pct)				Ultimate Analysis (Wt Pct)				
	M_{ad}	V_{ad}	FC_{ad}	A_{ad}	C_{ad}	H_{ad}	O_{ad}	N_{ad}	S_{ad}
Coke	1.31	4.81	80.46	13.42	85.68	0.18	0.27	0.96	0.30

M : moisture. V : volatile matter. FC : fixed carbon. A : ash. ad : air dried basis.

C. Softening, Melting, and Dropping Test

A specially designed high-temperature device^[33,34] was employed to perform the SMD test under simulated OY furnace conditions. The device was composed of a high-temperature furnace, a gas supply component, and a loading unit. The shrinkage displacement curve of the iron ore, the pressure drop curve of the gas passing through the iron ore bed, and the dropping weight curve can be obtained during the SMD test.

Firstly, the coke and prereduced mixed iron ore (V-Ti-bearing DRI) were placed into the graphite crucible sequentially, and the height of the prereduced DRI was recorded. Then, the graphite crucible was placed into the high-temperature furnace. After the vacuuming was completed, the power was turned on to make the device heat up and introduce reducing gas according to the predetermined program.

The surface temperature of the semi-coke bed of melter gasifier is about 850 °C, so the temperature from 0 to 850 °C was regarded as the preheating stage of the DRI during the SMD test, and the heating rate was set to a maximum of 10 °C/min. It takes about 2.5 h for the V-Ti-bearing DRI to move from the surface of the semi-coke bed to the tuyere. The heating rate for the SMD test at 850 to 600 °C should be 5 °C/min if the DRI is heated at a constant rate during the process. It should contain only CO and H₂ in the reducing gas, but some CO was replaced by Ar in consideration of experimental safety. The flow rate of reducing gas during the SMD test was set to 5 L/min. The schematic of the experimental process and detailed conditions involving SMD test are presented in Figure 1. Different parameters obtained from the SMD test were defined in Table III. The peak values of pressure drop (P_{P1} and P_{P2}) and gas permeability indexes (S_{D1} and S_{D2}) were used to characterize the resistance of reducing gas across the DRI bed. The higher the values of P_P and S_D , the more restrained the flow of reducing gas and the worse the gas permeability of the DRI bed. The detailed calculation formula was shown in References 33 and 34.

D. Characterization

After the SMD test, the interface between coke and slag was cut precisely with a curing agent inlay, and the cutting surface was polished. The mechanism of the interface formation and the reaction behavior of coke and slag were analyzed by SEM and EDS, respectively. SEM (JSM-7800F, JEOL) was mainly used to observe the micromorphology of residual slag and coke in the crucible reactor. The SEM instrument was equipped with EDS (80 mm² X-MaxN Silicon Drift Detector), and 15-kV accelerating voltage was selected for the microanalyzer operation. Slag was analyzed by an XRD analyzer (MAX2500PC X, Nippon koji co. LTD) coupled with a monochromator and a copper $K\alpha$ X-ray source. The accelerating voltage and current were 40 kV and 150 mA, respectively. The samples were scanned at 4 deg/min over an angular range of 15–90 deg with a scanning interval of 0.02 deg/step. Inductivity coupled plasma emission spectroscopy (ICP-OES, Optima 8000, PerkinElmer) was used to detect the vanadium content in the dropping iron and residual iron according to GB/T 38,441–2019.^[35] The chemical composition (CaO, SiO₂, MgO, Al₂O₃, FeO, and TiO₂) of the slag was detected by the wet chemical analysis method.^[36] Factsage (8.0) based on the Gibbs free energy minimization theory was applied to calculate the slag viscosity from slag composition using the embedded viscosity module and FToxid database.

III. RESULTS AND DISCUSSION

A. Prereduction Behavior of Mixed Iron Ore

The variations of weight and PRD of the mixed iron ores with time under the condition of isothermal reduction at 850 °C are shown in Figure 2. It can be seen that the variation trend of weight for the four reduction experiments are consistent, indicating that the reducibility of the iron ore is stable. With the increase of PRD, the reduction rate of the iron ore is reduced

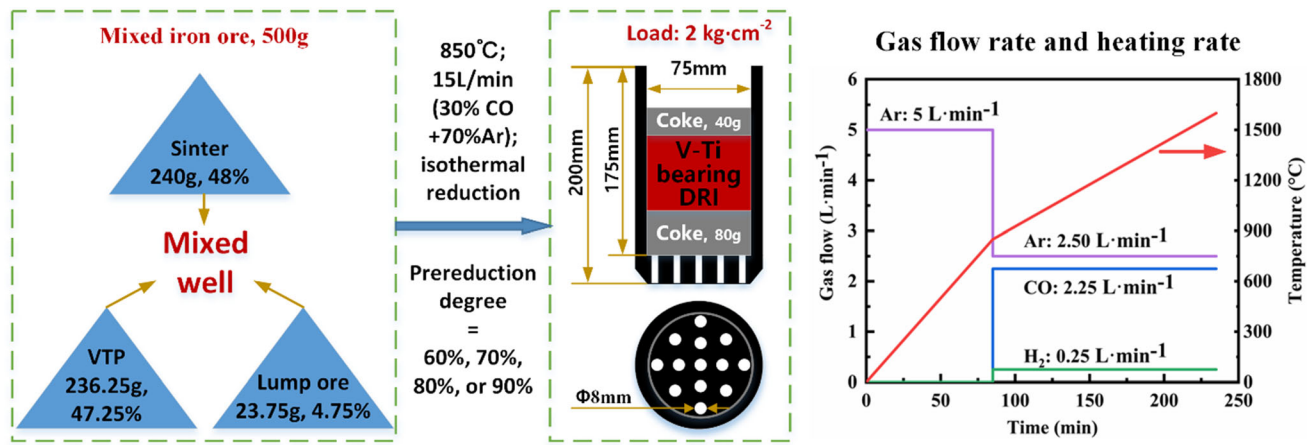


Fig. 1—Schematic diagram of the experimental process and conditions.

multiply. It takes about 17.22 min for the PRD of mixed iron ore increased from 60 to 70 pct, whereas the time is increased by 2.5 times, about 45.36 min when the PRD increases from 80 to 90 pct, occurring obvious reduction deceleration.^[37,38] This is homologous with the general observation of iron ore reduction.^[16,39] The process of reduction of iron ore can be divided into two stages, before and after the formation of the dense metal iron shell on the surface of iron ore particle. Before the formation of the metallic iron shell, the iron ore mainly undergoes phase transitions of $\text{Fe}_2\text{O}_3 \rightarrow \text{Fe}_3\text{O}_4$ and $\text{Fe}_3\text{O}_4 \rightarrow \text{FeO}$. Various defects such as interfaces, pores, and cracks exist in the formed Fe_3O_4 and FeO product layers, their inhibition on reduction is not conspicuous.^[40–42] After the metal iron shell is formed, the iron ore conforms to the phase transition of $\text{FeO} \rightarrow \text{Fe}$. Due to the dense metal iron shell, low diffusion coefficient of O atoms in the bcc Fe lattice, and higher thermodynamic nucleation barrier for Fe atoms, the reduction rate of iron ore is slowed down by nearly an order of magnitude.^[16,43]

Although the mixed iron ores are reduced under the same conditions in each experiment, the composition and phase of the mixed iron ore composed of sinter ore, pellet ore, and lump ore are different, so the PRD of different types of iron ore in each experiment is analyzed. The three kinds of ores are weighed, respectively, and their PRD are calculated as shown in Table IV. When the PRD of DRI is 60 pct, the PRD of sinter ore is the highest and the value is 64.12 pct; the second is lump ore, 61.55 pct; the PRD of VTP is lower than that of DRI and the value is 52.43 pct, all of which indicates that the reducibility of the VTP is inferior.^[44]

In order to further clarify the problem of slow reduction rate of VTP compared sinter ore and lump ore, the changes of phases both VTP and sinter ore were detected in different PRDs. The XRD spectra of the sinter ore and VTP before and after prereduction treatment are shown in Figure 3. The initial phase of sinter is mainly Fe_3O_4 and gangue $\text{CaAl}_2\text{Si}_2\text{O}_8$, while the initial phase of VTP is Fe_2O_3 . The phases containing vanadium and titanium in VTP are not detected due to the overpowering iron oxide diffraction peaks. When the

PRD of DRI is 60 pct, the sinter is basically reduced to FeO and contains a small amount of Fe, while the VTP mainly contains FeO and Fe_3O_4 , and no Fe diffraction peaks are observed. When the PRD further reaches 90 pct, the main phase of the sinter is transformed into Fe, containing a small amount of FeO ; although the VTP is also reduced to produce Fe at this time, some obvious Fe_3O_4 and FeO diffraction peaks are found. This indicates that the reduction rate of VTP is significantly lower than that of sinter, which is consistent with the previous results.

B. Effect of PRD on the Softening Behavior and SMD Temperature Parameters of V–Ti-Bearing DRI

There is an apparent regularity of the shrinkage curve of DRI bed, which can be divided into two stages at before and after the shrinkage ratio of 70 pct, as shown in Figure 4. In stage 1, the shrinkage ratio ranging from 10 to 70 pct, the shrinkage change of DRI bed decreases with the increased PRD of DRI at the same temperature, which verifies the foregoing conclusion that the DRI particles with higher PRD have a thicker iron shell, effectively dwindling the DRI creep at high temperature.^[21–23] In stage 2, the shrinkage ratio of more than 70 pct, an opposite change between the shrinkage and PRD is observed, except for the DRI with 60 pct PRD due to its rapid contraction. This may be related to the melting of the iron shell of DRI with high PRD when the temperature exceeds 1400 °C, the specific causes have yet to be further studied.

The influence of PRD on the SMD temperature parameters of the V–Ti-bearing DRI is presented in Figure 5. With the increasing PRD from 60 to 90 pct, the start temperatures of softening (T_{10}) of the four V–Ti-bearing DRIs have little changes, while the end temperatures of softening (T_{40}) increase significantly, from 1226 °C to 1286 °C. It is due to the fact that the DRI with high PRD has thicker metal iron shell and higher compressive strength, which effectively resists the load shrinkage of the bed at high temperature and improves its T_{40} .^[23] The bed shrinkage before T_{10} is mainly attributed to the sintering between DRI

Table III. Parameters Obtained from SMD Test to Characterize the Softening, Melting, and Dropping Properties of DRI

Para	Significance	Para	Significance
T_{10}	temperature of DRI shrinkage reaching 10 pct, °C	ΔT_1	softening interval, $T_S - T_{10}$
T_{40}	temperature of DRI shrinkage reaching 40 pct, °C	ΔT_2	melting drop interval, $T_d - T_S$
T_S	temperature of pressure drop first reaching 0.5 kPa, °C	ΔT_3	soft melting interval, $T_d - T_{10}$
T_d	temperature of DRI first dropping from crucible, °C	ΔT_{de}	dropping interval, $T_{de} - T_d$
T_{de}	temperature of DRI no longer dropping, °C	ΔT_f	slag foaming interval, $T_f - 1600^\circ\text{C}$
T_f	temperature of pressure drop of bed rising again, °C		

Reprinted with permission from Ref. [33].

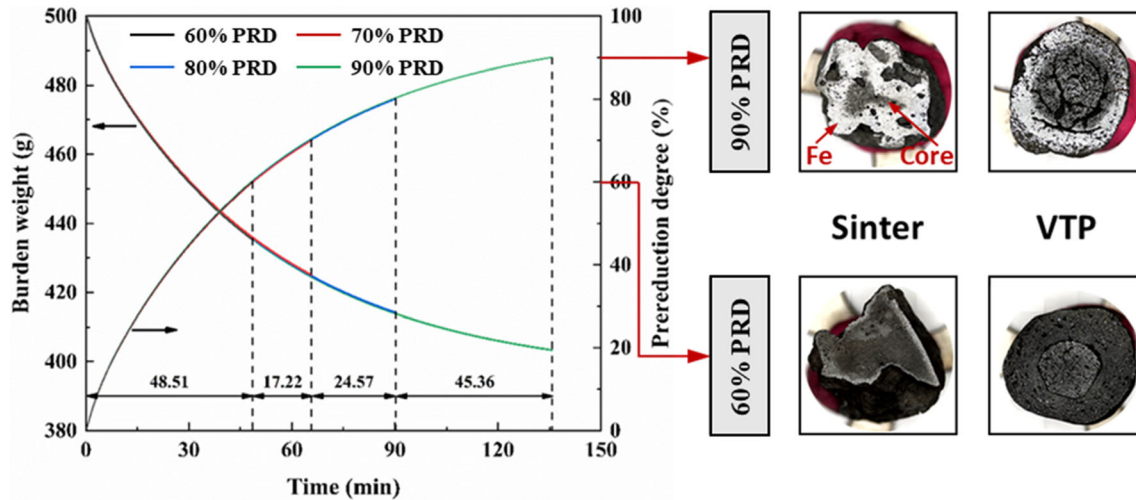


Fig. 2—Weight loss and prereduction degree as a function of time of the mixed iron ore for isothermal reduction at 850 °C.

Table IV. Actual weight Loss and PRD of Each Kind of Iron Ore After the Prereduction Treatment

PRD of the DRI (Pct)	Sinter Ore		VTP		Lump ore	
	Loss (g)	PRD (Pct)	Loss (g)	PRD (Pct)	Loss (g)	PRD (Pct)
60	31.95	64.12	28.34	52.43	2.06	61.55
70	37.65	74.85	33.63	62.08	2.47	71.17
80	43.22	85.20	39.20	72.04	2.89	80.96
90	48.35	94.86	44.98	82.51	3.29	90.23

particles, which largely depends on the DRI particle size. Therefore, the T_{10} of V-Ti-bearing DRI with different PRDs stays the same.^[37] As a result, the softening range (ΔT_1) of the bed is enlarged by 17.7 °C for every 10 pct increase in the PRD.

Then the melting temperature (T_S) and dropping temperature (T_d) are also raised with increasing PRD. There is a strong linear relationship between T_S and PRD with a 10 pct increase in PRD leading to a 37 °C increase in T_S . The reason for the appearance of T_S is that the melting point of iron shell of DRI is decreased under the effect of carburizing, triggering its melting and breaking. The liquid initial slag rich in FeO also flows out from the iron shell, which leads to the blockage of the gas channel of the bed layer and the sharp rise of the pressure drop.^[45,46] Since the compressive strength of the DRI with high PRD is larger, it is melted and broken at a higher temperature. And the DRI with high PRD

contains less FeO for slag forming, which increases the initial slag generation temperature. Consequently, T_S increases obviously with the increase of PRD. However, the growth rate of T_d is decreased with the increase of PRD, and the T_d barely grows as the PRD increases from 80 to 90 pct (see Sect. 3.5 for reasons). To sum up, the growth of PRD increases the ΔT_1 , shrinks the ΔT_2 and moves it to the high-temperature zone, resulting in the expansion of the ΔT_3 , which should be favorable for the smelting of vanadium-titanium magnetite.^[24]

C. Effect of PRD on the Liquid Permeability of V-Ti-Bearing DRI

The PRD of DRI also has a significant impact on the permeability of liquid iron and slag through the coke layer at high temperature. Figure 6 shows the morphology and weight of dropping iron and slag obtained from

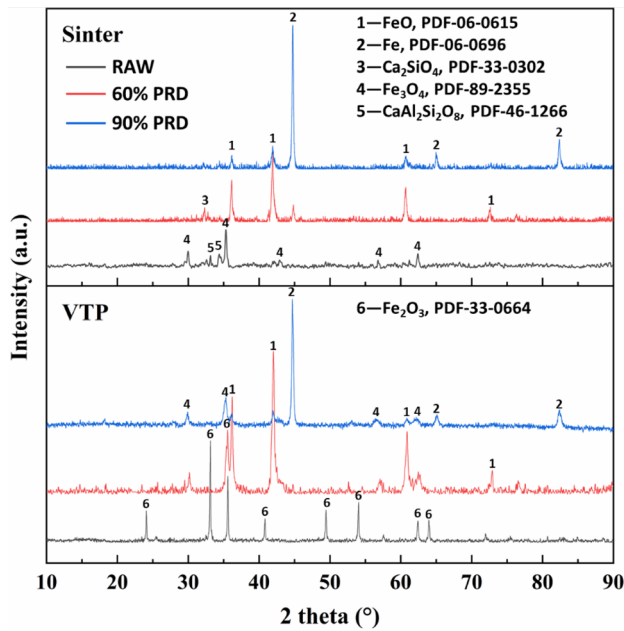


Fig. 3—XRD spectra of the sinter ore and VTP before and after pre-reduction treatment.

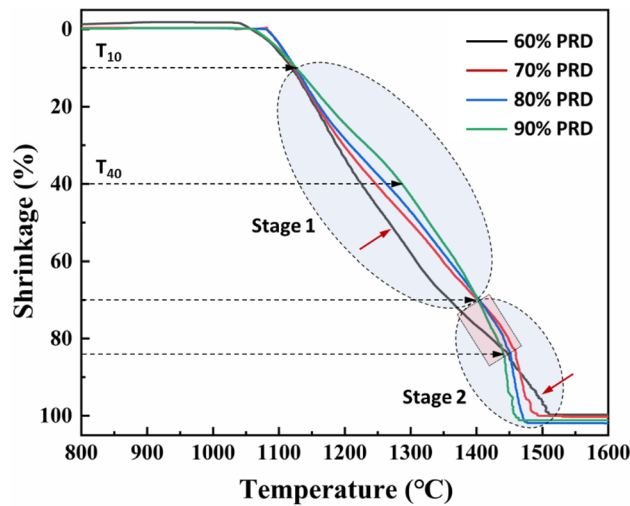


Fig. 4—Shrinkage rate of the V-Ti-bearing DRI with different PRDs as a function of temperature.

the DRI with different PRDs. It can be seen that the amounts of dropping iron and slag are diminished rapidly with the increase of PRD of DRI. The dropping rates of iron and slag are as high as 96.7 pct and 86.95 pct when the PRD is 60 pct. At this moment, the residual iron is almost invisible in the crucible reactor, and a small amount of residual slag adhere to the surface of the coke in film. It seems to imply that the slag and coke have good wetting properties, but we all know that ordinary metallurgical slag and coke do not wet each other. This is attributed to the formation of TiC between titanium slag and coke and precipitation on the

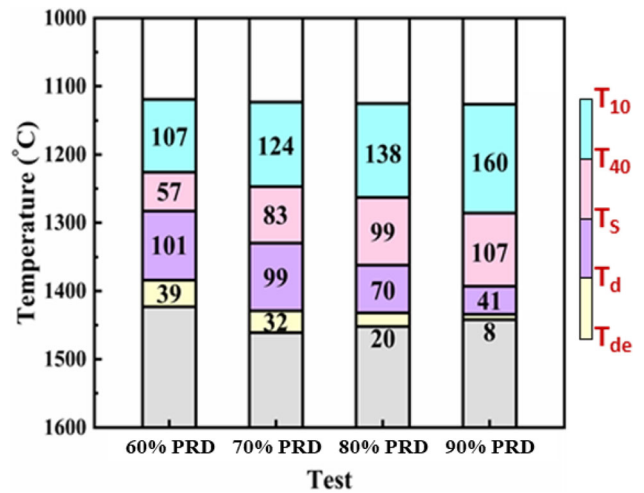


Fig. 5—Effect of PRD on the SMD temperature parameters of V-Ti-bearing DRI.

coke surface, which enhances the adhesion of coke surface to slag, greater than the cohesion of slag,^[33,34] so that the slag is bonded to the coke surface.

When the PRD of DRI gets 70 pct, there are obviously agglomerated iron and slag in the interspace of coke particles. Most of slag exists in the upper coke layer, and the iron occurs in the lower coke layer. This is because the viscosity of the liquid slag is high (0.1 to 0.5 Pa·s), which hinders the ascent of reducing gas, then the reducing gas also gives the liquid slag an upward force.^[47,48] Under the action of the interface tension between slag and coke, slag is stably deposited in the upper coke layer. While the viscosity of the molten iron is small (0.01 to 0.05 Pa·s),^[49] which has little effect on airflow, and flows downward under the action of gravity, thereby realizing the separation of iron and slag.

Since the PRD of DRI reaches 80 pct and 90 pct, the drop rates of the liquid iron and slag are further decreased (see Section III-B for specific reasons). At that moment, millimeter-scale bubbles can be observed clearly from the profile of residual slag. It indicates that the slag has foamed, and subsequent results about the pressure drop also illustrate this phenomenon.

The XRD analysis shows that the dropping slag obtained by oil quenching is completely glassy, without the characteristic diffraction peaks of high-melting point phases such as TiC and VC (Figure 7). It means that little TiC is formed before the slag dropping temperature, or the TiC generated is limited to the slag-coke interface, and does not form a solid-liquid mixture with the slag and drop together. However, the XRD result of the residual slag after acid leaching (5 wt pct hydrochloric acid solution, electromagnetic stirring 3 h)^[50] presents obviously TiC diffraction peaks, indicating that a certain amount of TiC is generated in the residual slag. The presence of TiC greatly improves the viscosity of the residual slag, and is the main contributor for slag foaming.^[25-29]

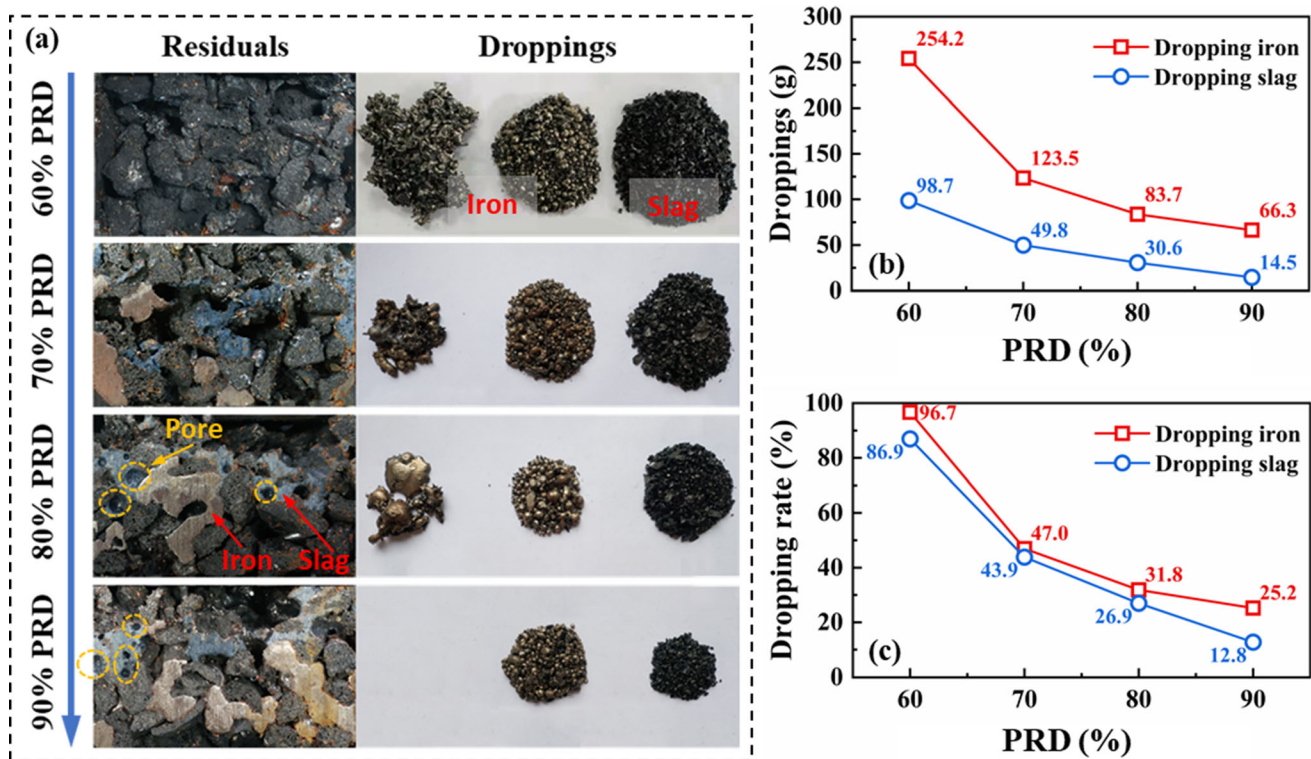


Fig. 6—Morphology and weight of dropping iron and slag obtained from the DRI with different PRDs, (a) morphology of iron and slag, (b) weight of dropping iron and slag, (c) dropping rate of iron and slag.

Further, the micromorphology and distribution of TiC in the residual slag are acquired by SEM-EDS, as presented in Figure 8. There is evident white reaction layer at the interface between the residual slag and coke under the four PRD conditions, which is formed by the aggregation of white granular substances, and its thickness ranges from hundreds of nanometers to tens of microns. From the map and point scanning analysis, the main elements constituting the reaction interface are Ti, C, and O. Therefore, it can be concluded that these white granular substances are TiC produced from the reduction of titanium-containing slag by coke. However, the particle size of these TiC particles is basically maintained at the nanometer level, which is much smaller than previous studies (several micrometers to tens of micrometers), and not dispersed and suspended in the slag. With the increase of the PRD of DRI, the TiC granules at the interface of the slag and coke are continued to increase. The coke boundary is significantly eroded, especially near the pores as the PRD reaches 90 pct. The TiC granules not only accumulate densely at the interface of slag and coke but also diffuse into the slag gradually.

The vanadium content and yield in the residual iron and dropping iron as a function of the PRD of DRI are illustrated in Figure 9. The vanadium contents in the residual iron and dropping iron are improved with the increasing PRD. There are two reasons for it, one is that the content of iron oxide is less as the DRI has a higher PRD. According to thermodynamic analysis, the vanadium oxide in the V-Ti-bearing DRI can be reduced by

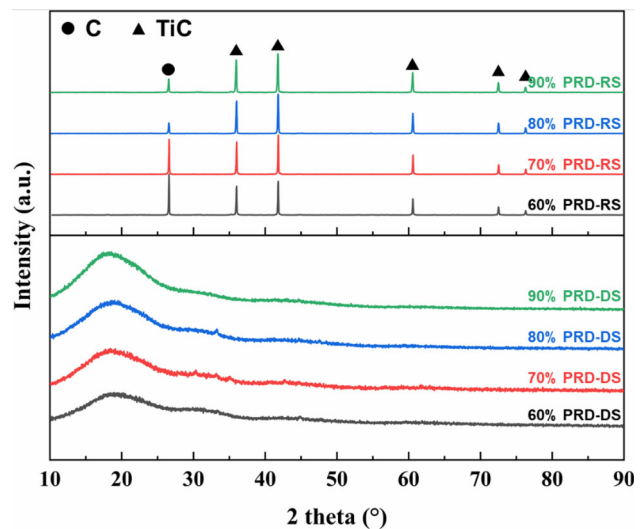


Fig. 7—XRD spectra of dropping and residual slags obtained from the DRI with different PRDs (DS is the dropping slag, RS is the residual slag).

CO or C and dissolved in the molten iron only after the iron oxide is reduced completely. Therefore, the reduction of vanadium oxide in the DRI with high PRD is moved up. Second, the dropping temperature is also improved significantly with the increasing PRD, which prolongs the reduction time of DRI at high temperature, so that more vanadium oxides are reduced into the molten iron.

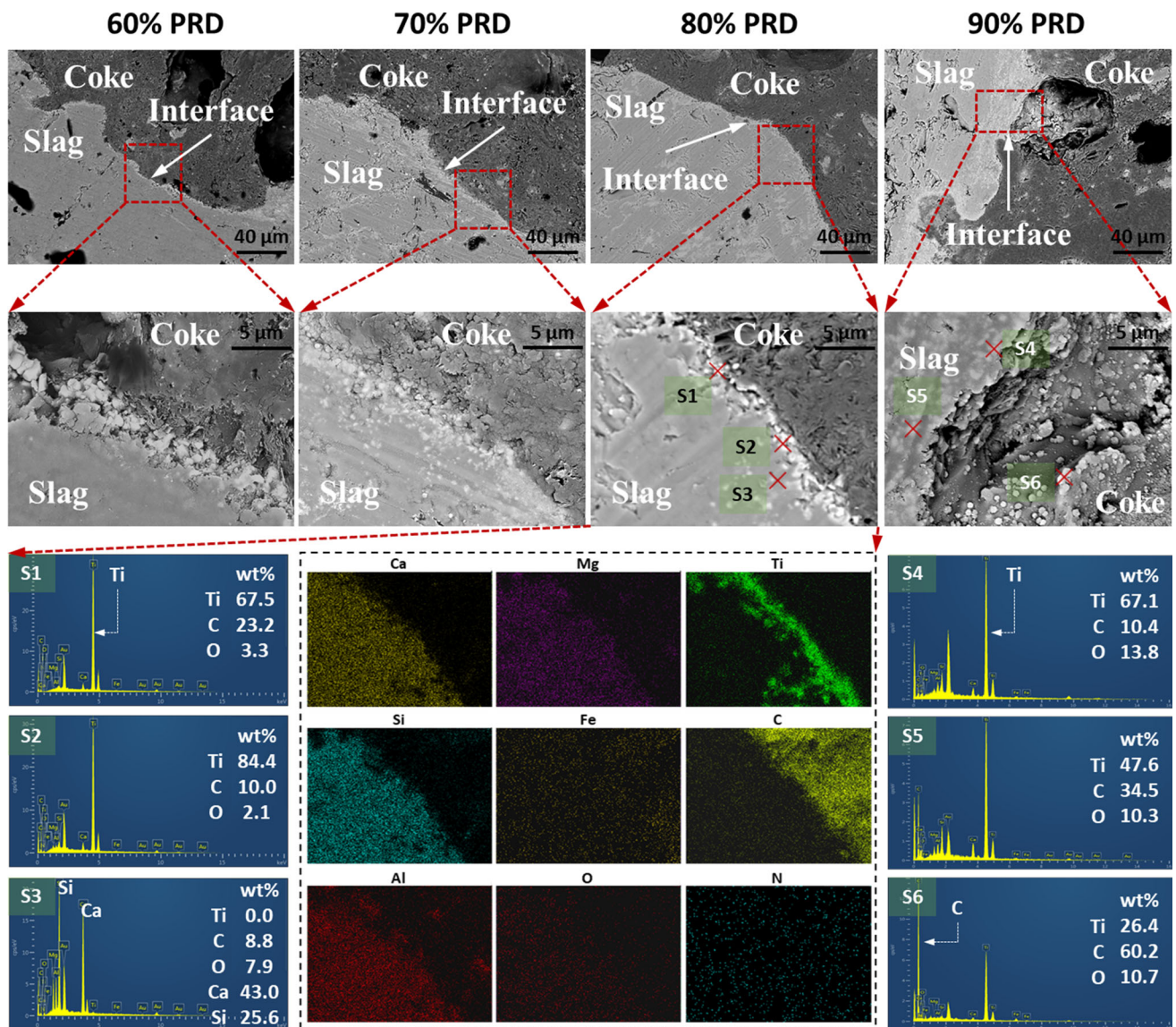


Fig. 8—Microstructure and elemental distribution of residual slag obtained from the DRI with different PRDs.

In addition, it is also noted that the vanadium yield in the residual iron increases with the enhancement of the PRD of DRI, while the vanadium yield in the dropping iron is decreased, which is caused by the decrease of dropping iron with the increased PRD. However, the sum of vanadium yield in the residual iron and dropping iron is far less than 100 pct, which displays that the vanadium oxide contained in V–Ti-bearing DRI is not completely reduced in the cohesive zone of the semi-coke bed.^[33,34]

D. Effect of PRD on the Gas Permeability of V–Ti-Bearing DRI

The pressure drop curves of V–Ti-bearing DRI with different PRDs are presented in Figure 10. All of them can be divided into two sections, stage I and stage II. Stage I is initiated from T_s of the DRI bed. Under the effect of carburizing, the initial slag in the iron shell

flows out, resulting in a blockage of the gas channel of the bed layer. The pressure drop increases rapidly and then decreases after reaching a maximum value. This is because the slag viscosity is decreased with the increasing temperature, and its hindrance to gas is impaired. It is worth noting that all the experiments show a common characteristic, the reduced DRI begins to drop since the pressure drop falls back to a certain value. This is a counterintuitive finding, it is not liquid iron and slag dropping that leads to the decrease of the bed pressure drop, but rather the slag viscosity decreases with the increased temperature, resulting in the decrease of pressure drop, and the reduced DRI drops under gravity.^[33,34]

The chemical composition of the dropping slag is shown in Table V. The FeO content in dropping slag decreases significantly from 7.46wt pct to 2.44wt pct with increasing PRD of DRI. However, there are increases in the contents of CaO, SiO₂, MgO, Al₂O₃,

and TiO_2 . The basicity of dropping slags is approximately remained constant, about 1.04, which is close to that of theoretical final slag.

The viscosity of the dropping slag is calculated by above slag composition using Factsage 8.0 (Figure 11). With the increase in the PRD of DRI, the viscosity of the dropping slag is improved. But there is only a little

difference in the viscosity of the dropping slags at the temperature when the dropping occurs, and is maintained at about 0.15 Pa·s. It seems to indicate that the DRI is only dropped after the slag viscosity reduces to a certain value. This again corroborates the conclusion from Figure 10. The slag viscosity is decreased with the increasing temperature, resulting in the decrease of pressure drop, and the reduced DRI drops under gravity. This is also the reason why the T_d is raised with the improved PRD of DRI.

After the reduced DRI drops for a while, the pressure drop curve suddenly rises again, entering the Stage II (Fig. 10). The starting point of the second step rise in pressure drop is named as the slag foaming temperature (T_f), in that the pressure drop curve after this temperature shows a serrated change, indicating a strong foaming phenomenon appears in the molten slag. The drastic fluctuation of the pressure drop is only triggered by the rapid generation, rise, bursting and dissipation of the foaming slag in the gap of coke particles.

It is also noted that the T_{de} and T_f are almost coincident, except for the DRI with 60 pct PRD (Figure 5), but a large amount of iron and slag is still remained in the crucible reactor as the DRI stops dropping. This shows that the secondary rise of the pressure drop inhibits the DRI dropping, leading to an advance of T_{de} .^[33,34] However, there is a large difference between T_{de} and T_f as the DRI with 60 pct PRD, it is due to that the dropping performance of the DRI is good at this time, and the slag drops almost completely before foaming.^[33] The above is the reasons why the

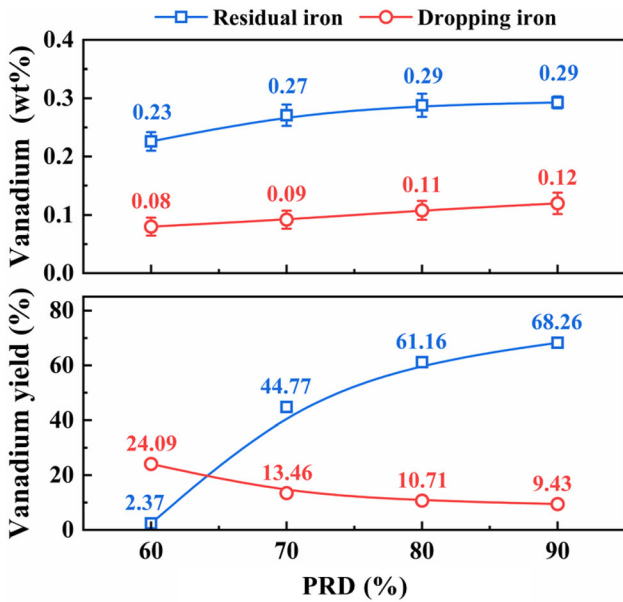


Fig. 9—Vanadium content and yield in the residual and dropping iron as a function of the PRD of DRI.

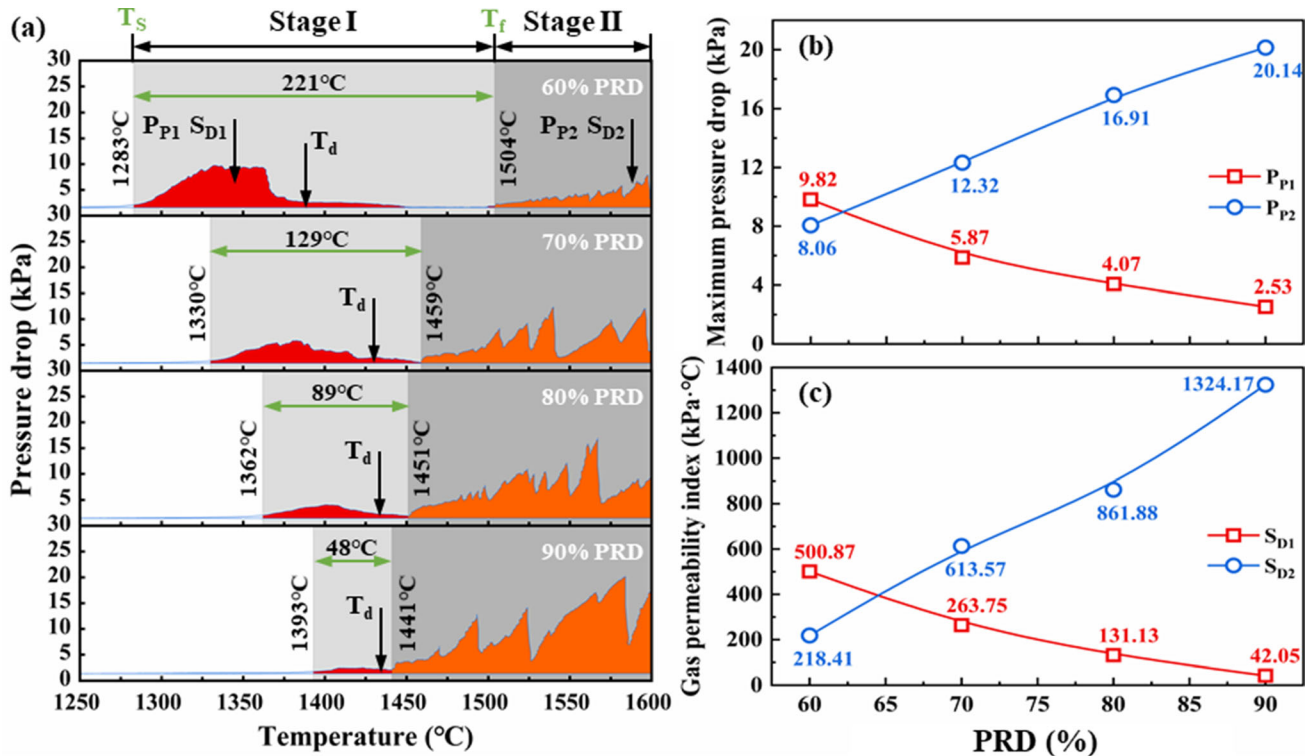


Fig. 10—Pressure drop and gas permeability index of V-Ti-bearing DRI under different PRDs, (a) pressure drop curve, (b) maximum pressure drop, (c) gas permeability index.

Table V. Chemical Composition of Residual Slag, Dropping Slag, and Theoretical Slag

	PRD (pct)	CaO (wt pct)	SiO ₂ (wt pct)	MgO (wt pct)	Al ₂ O ₃ (wt pct)	FeO (wt pct)	TiO ₂ (wt pct)	R_2
Dropping Slag	60	27.39	26.19	9.25	11.28	7.46	18.43	1.05
	70	27.65	26.49	9.87	11.81	5.36	18.82	1.04
	80	27.97	26.84	9.96	12.23	3.99	19.01	1.04
	90	28.42	27.37	10.14	12.41	2.44	19.22	1.04
Theoretical Slag	—	31.15	29.30	9.19	11.31	—	19.05	1.06

$$R_2 = \text{wt pct (CaO)}/\text{wt pct (SiO}_2\text{)}.$$

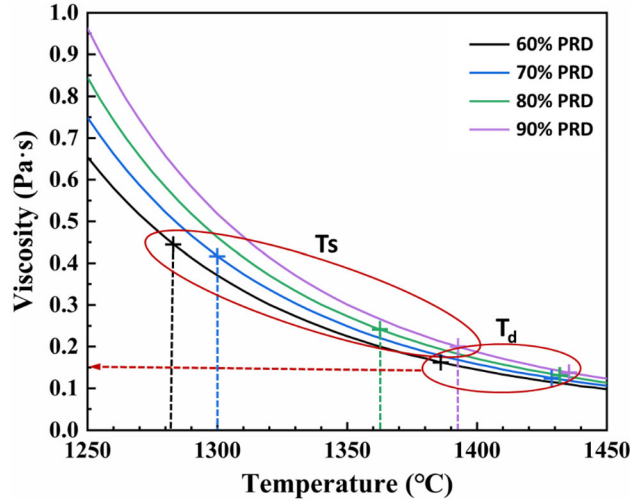


Fig. 11—Theoretical viscosity of dropping slag of V-Ti-bearing DRI with different PRDs.

drop rates of iron and slag are decreased, and the permeability of the DRI bed is deteriorated with the increasing PRD. In other words, the increasing PRD of DRI decreases the FeO in slag, making it lose its ability to inhibit the formation of TiC [$2(\text{FeO}) + \text{TiC} = (\text{TiO}_2) + 2\text{Fe} + \text{C}$], resulting in slag foaming. It leads to the sharp rise of bed pressure drop again, inhibiting the dropping of iron and slag.

At Stage I, the maximum pressure drop (P_{P1}) and gas permeability index (S_{D1}) are negatively correlated with the PRD of DRI. The P_{P1} is decreased from 9.82 to 2.53 kPa, and S_{D1} is decreased from 500.87 kPa °C to 42.05 kPa °C when the PRD of DRI is increased from 60 to 90 pct. In addition, the temperature range of Stage I is also shrunk with the increasing PRD. As mentioned above, the rise of T_S is attributed to the improvement of the compressive strength of the DRI and the increase of the formation temperature of the initial slag with the increasing PRD. The decrease of T_f is due to the decrease of FeO in the initial slag, which accelerates the reduction of TiO₂ to TiC and slag foaming.

Although the viscosity of the molten slag is increased with the increase of PRD, but the T_S of the DRI go up significantly. Therefore, under the influence of temperature, the viscosity of the initial slag generated by the DRI with high PRD is smaller than that generated by the DRI with low PRD (Figure 11). It is weak for the

impact of the initial slag generated by the DRI with high PRD on the gas flow, resulting in a decrease of P_{P1} with the increased PRD. Accordingly S_{D1} is also decreased due to the narrowing of stage I. Under the conditions of this research, the P_{P1} and S_{D1} are declined by 0.24 kPa and 15.29 kPa °C for every 1 pct increase in the PRD.

At Stage II, P_{P2} and S_{D2} are increased from 8.06 kPa and 218.41 kPa °C to 20.14 kPa and 1324.17 kPa °C for the PRD increasing from 60 to 90 pct. On the one hand, the reduction of TiO₂ in the slag is accelerated by the increased PRD, and the formation of TiC is raised, which leads to an increase in the viscosity of the slag.^[30,31] Since the pressure drop at stage II is much larger than that of stage I, stage II is the decisive stage for the gas permeability of the DRI bed. Increasing the PRD of DRI will deteriorate the gas permeability of the bed, which is not conducive to the OY furnace smelting vanadium-titanium magnetite.

IV. CONCLUSIONS

In this paper, it was investigated of the effect about increased pre-reduction degree (PRD) from 60 to 90 pct on the softening, melting, and dropping behavior of V-Ti-bearing DRI under simulated OY furnace conditions. The V-Ti-bearing DRI with higher PRD is more likely to foam in the semi-coke bed, resulting in fluctuation of pressure drop, which is not conducive to OY furnace smelting vanadium-titanium magnetite, and the main findings are summarized as follows,

1. The improved PRD increases the iron shell thickness and creep resistance of the V-Ti-bearing DRI, resulting in an increase in the end temperature of softening (T_{40}). Meanwhile, the FeO content in the DRI for slag formation is decreased with the improved PRD, which increase the melting point and viscosity of the initial slag, increasing the DRI melting temperature (T_S) and dropping temperature (T_d). The DRI softening interval (ΔT_1) is expanded from 107 °C to 160 °C, and the melting interval (ΔT_2) is shrunk from 101 °C to 41 °C when the PRD is increased from 60 to 90 pct.
2. TiC formation and slag foaming are accelerated with the increased PRD (60 to 90 pct) of DRI, the slag foaming temperature (T_f) is declined from 1504 °C to 1441 °C, and the dropping rates of molten iron and slag are reduced from 96.7 pct and 86.9 pct to 25.2

pct and 12.8 pct, respectively, deteriorating the liquid permeability of the V–Ti-bearing DRI. While the vanadium contents in the dropping iron and residual iron are improved with the increased PRD.

- At the stage I of the pressure drop curve, the maximum pressure drop (P_{Peak}) and gas permeability index (S_D) are decreased, respectively, from 9.82 kPa and 500.87 kPa °C to 2.53 kPa and 42.05 kPa °C with the increasing PRD, while the P_{Peak} and S_D at stage II are increased from 8.06 kPa and 218.41 kPa °C to 20.14 kPa and 1324.17 kPa °C due to the generated TiC and slag foaming. It is not recommended to use DRI with excessive PRD for OY furnace smelting vanadium–titanium magnetite.

ACKNOWLEDGMENTS

The work is supported by the National Natural Science Foundation of China (Project No. U2003215) and Chongqing Talent Program (Project No. cstc2021ycjh-bgzxm0108). The authors also thank Xinjiang Bayi Iron & Steel Co., Ltd for providing samples used in the research.

CONFLICT OF INTEREST

On behalf of all authors, the corresponding author declare that they have no conflict of interest.

REFERENCES

- Q. Tu and E.G. Hertwich: *J. Ind. Ecol.*, 2021, vol. 26, pp. 704–17.
- P. Li, X. Li and F. Li: *J. Clean Prod.*, 2020, vol. 266. <https://doi.org/10.1016/j.jclepro.2020.121732>.
- H. Trollip, B. McCall, and C. Bataille: *Clim. Policy*, 2022, vol. 22, pp. 236–47.
- S. Yao, B. Song, S. Wu, M. Kou, Y. Hu, and H. Zhou: *Ironmaking Steelmaking*, 2021, vol. 48, pp. 693–702.
- S. Wu, J. Xu, J.I. Yagi, X. Guo, and L. Zhang: *ISIJ Int.*, 2011, vol. 51, pp. 1344–52.
- C.A. Myers, T. Nakagaki, and K. Akutsu: *Int. J. Greenh. Gas Control*, 2019, vol. 87, pp. 100–11.
- L. Holappa: *Metals*, 2020, vol. 10. <http://doi.org/https://doi.org/10.3390/met10091117>.
- European Commission: ULCOS top gas recycling blast furnace process (ULCOS TGRBF), 1st ed., Publications Office, 2014. <https://data.europa.eu/doi/https://doi.org/10.2777/59481>.
- L.H. Han, Y.H. Li, L.N. Han, Y.X. Liu, W.Q. Huang, L. Cao, S.C. Qi, X. Guan, and J.L. Yuan: *J. Iron Steel Res. Int.*, 2022, vol. 29, pp. 907–13.
- X.S. Zhang, Z.S. Zou, and Z.G. Luo: *J. Iron Steel Res. Int.*, 2019, vol. 26, pp. 567–77.
- J. Sun, S. Wu, M. Kou, W. Shen, and K. Du: *ISIJ Int.*, 2014, vol. 54, pp. 43–48.
- X. Liu, C. Liu, B. Wang, and F. Ye: *J. S. Afr. Inst. Min. Metall.*, 2019, vol. 119, pp. 445–52.
- M. Kou, S. Wu, K. Du, W. Shen, X. Ma, M. Chen, and B. Zhao: *Jom*, 2015, vol. 67, pp. 459–66.
- W.L. Zhan, K. Wu, Z.J. He, Q.H. Liu, and X.J. Wu: *J. Iron Steel Res. Int.*, 2015, vol. 22, pp. 1078–84.
- S. Wu, J. Zhang, M. Kou, B. Wen, H. Zhou: *9th International Symposium on High-Temperature Metallurgical Processing, Phoenix, AZ:701–14*.
- S.H. Kim, X. Zhang, Y. Ma, I.R. Souza Filho, K. Schweinar, K. Angenendt, D. Vogel, L.T. Stephenson, A.A. El-Zoka, J.R. Mianroodi, M. Rohwerder, B. Gault and D. Raabe: *Acta Mater.*, 2021, vol. 212, pp. 116933–38.
- R. Xu, H. Zheng, W. Wang, J. Schenk, A. Bhattacharyya, Z. Xue, and M. Song: *Int. J. Coal Prep. Util.*, 2018, vol. 41, pp. 216–32.
- X. Fan, K. Jiao, J. Zhang, and R. Wang: *ISIJ Int.*, 2021, vol. 61, pp. 1758–67.
- C. Srishilan and A.K. Shukla: *Metall. Mater. Trans. B*, 2019, vol. 50B, pp. 312–23.
- C. Srishilan, A. Vivek, and A.K. Shukla: *ISIJ Int.*, 2020, vol. 60, pp. 656–61.
- K.I. Ohno, H. Konishi, T. Watanabe, S. Ishihara, S. Natsui, T. Maeda, and K. Kunitomo: *ISIJ Int.*, 2020, vol. 60, pp. 1520–27.
- Z.Y. Wang, J.L. Zhang, K.X. Jiao, and Z.J. Liu: *Steel Res. Int.*, 2018, vol. 89, pp. 1700363–66.
- Y.Z. Pan, H.B. Zuo, B.X. Wang, J.S. Wang, G. Wang, Y.L. Liu, and Q.G. Xue: *Ironmaking Steelmaking*, 2020, vol. 47, pp. 322–27.
- F.R. Silva, L.R. Lemos, P. De Freitas Nogueira and M. Bressan: *Metall. Mater. Trans. B*, 2021, vol. 52B, pp. 69–76.
- H. Wang, G. Qiu, and Q. Deng: *Metal. Int.*, 2012, vol. 17, pp. 22–26.
- W. Zhao, M.S. Chu, H.T. Wang, Z.G. Liu, and Y.T. Tang: *Int. J. Miner. Metall. Mater.*, 2016, vol. 23, pp. 501–10.
- Z. Chang, J. Zhang, and X. Ning: *Fuel*, 2019, vol. 253, pp. 32–39.
- H. Xie, W. Yu, Z. You, X. Lv, and C. Bai: *Metals*, 2019, vol. 9, pp. 395–96.
- W. Zhao, M. Chu, Z. Liu, H. Wang, J. Tang, and Z. Ying: *Metall. Mater. Trans. B*, 2019, vol. 50B, pp. 1878–95.
- G.H. Zhang, Y.L. Zhen, and K.C. Chou: *ISIJ Int.*, 2015, vol. 55, pp. 922–27.
- Y.X. Liu, J.L. Zhang, G.H. Zhang, K.X. Jiao, and K.C. Chou: *Ironmaking Steelmaking*, 2017, vol. 44, pp. 609–18.
- Y.Z. Pan, A.J. Zhang, L. Lin, J.S. Wang, H.X. Feng, Q.S. Lin: *10th International Symposium on High-Temperature Metallurgical Processing, San Antonio, TX:523–30*.
- C. Yin, S. Zhang, X. Yang, W. Yuan, W. Yu, L. Wen, T. Li, and C. Bai: *Metall. Mater. Trans. B*, 2021, vol. 52B, pp. 4096–4108.
- C. Yin, S. Zhang, Y. Guo, L. Wen, and C. Bai: *ISIJ Inter.*, 2022, vol. 62, pp. 1777–84.
- National Standard (Standardization Administration of China, 2019). <https://kns.cnki.net/kcms/detail/detail.aspx?FileName=SCSF00061542&DbName=SCSF>. Accessed 31 December 2019.
- National Standard (Standardization Administration of China, 2008). <https://kns.cnki.net/kcms/detail/detail.aspx?FileName=SCSF00012632&DbName=SCSF>. Accessed 13 May 2008.
- P. Kaushik and R.J. Fruehan: *Ironmaking Steelmaking*, 2006, vol. 33, pp. 507–19.
- A.A. Adetoro, H. Sun, S. He, Q. Zhu, and H. Li: *Metall. Mater. Trans. B*, 2018, vol. 49B, pp. 846–57.
- Vemdrame Flores, O. Matos, A. Lima da Silva and M. Covichev Bagatini: *Metall. Mater. Trans. B*, 2021, vol. 52B, pp. 1–23.
- R. Barlow and P.J. Grundy: *J. Mater. Sci.*, 1969, vol. 4, pp. 797–801.
- J. Takada and M. Adach: *J. Mater. Sci.*, 1986, vol. 21, pp. 2133–37.
- H. Hagi: *Metall. Mater. Trans. JIM*, 1994, vol. 35, pp. 112–17.
- S. H. Kim, X. Zhang, Y. Ma, I. R. Souza, K. Schweinar, K. Angenendt, D. Vogel, L. T. Stephenson, A. A. El-Zoka, J. R. Mianroodi, M. Rohwerder, B. Gault and D. Raabe: *Acta Materialia*, 2021, vol. 212. <https://doi.org/10.1016/j.actamat.2021.116933>.
- S.M. Jung: *ISIJ Inter.*, 2014, vol. 54, pp. 781–90.
- P.F. Nogueira and R.J. Fruehan: *Metall. Mater. Trans. B*, 2006, vol. 37B, pp. 551–58.
- P.F. Nogueira and R.J. Fruehan: *Metall. Mater. Trans. B*, 2005, vol. 36B, pp. 583–90.
- Z. Yan, R.G. Reddy, X. Lv, Z. Pang, and C. Bai: *Metall. Mater. Trans. B*, 2019, vol. 50B, pp. 251–61.
- X. Yu and Y. Shen: *Metall. Mater. Trans. B*, 2018, vol. 49B, pp. 2370–88.
- X.Y. Teng, G.H. Min, H.L. Liu, and Y.F. Ye: *Metall. Mater. Trans. B*, 2001, vol. 23, pp. 401–06.

50. K.H. Wu, G.H. Zhang, H.P. Gou, and K.C. Chou: *Vacuum*, 2018, vol. 151, pp. 51–60.

Publisher's Note Springer Nature remains neutral with regard to jurisdictional claims in published maps and institutional affiliations.

Springer Nature or its licensor (e.g. a society or other partner) holds exclusive rights to this article under a publishing agreement with the author(s) or other rightsholder(s); author self-archiving of the accepted manuscript version of this article is solely governed by the terms of such publishing agreement and applicable law.